Synergetic boost of functional properties near critical end points in antiferroelectric systems

Vida Jurečič[1,2], Lovro Fulanović[3], Jurij Koruza[4], Vid Bobnar[1,2] and Nikola Novak[1,*]

[1] *Condensed Matter Physics Department, Jožef Stefan Institute, Jamova cesta 39, SI-1000 Ljubljana, Slovenia*

[2] *Jožef Stefan International Postgraduate School, Jamova cesta 39, SI-1000 Ljubljana, Slovenia*

[3] *Department of Materials and Earth Sciences, Nonmetallic Inorganic Materials, Technical University of Darmstadt, 64287 Darmstadt, Germany*

[4] *Institute for Chemistry and Technology of Materials, Graz University of Technology, A-8010 Graz, Austria*

*Corresponding author: nikola.novak@ijs.si

The increase of the dielectric permittivity with an electric field and enhanced energy storage properties make antiferroelectrics very attractive for high-power electronic applications needed in emerging green energy technologies and neuromorphic computing platforms. Their exceptional functional properties are closely related to the electric field-induced antiferroelectric↔ferroelectric phase transition, which can be driven toward a critical end point by manipulation with an external electric field. The critical fluctuation of physical properties at the critical end point in ferroelectrics is a promising approach to improve their functional properties. Here we demonstrate the existence of two critical end points in antiferroelectric ceramics with a ferroelectric-antiferroelectric-paraelectric phase sequence, using the model system $Pb_{0.99}Nb_{0.02}[(Zr_{0.57}Sn_{0.43})_{0.92}Ti_{0.08}]_{0.98}O_3$. The critical fluctuation of the dielectric permittivity in the proximity of the antiferroelectric-to-paraelectric critical end point is responsible for the strong enhancement of the dielectric tunability (by a factor of > 2) measured at ≈395 K. The enhancement of the energy storage density at ≈370 K is related to the proximity of the ferroelectric-to-antiferroelectric critical end point. These findings open new possibilities for material design and pave the way for the next generation of high-energy storage materials.

I. INTRODUCTION

Antiferroelectrics (AFEs) are a subgroup of dielectric materials with spontaneous polarization in which adjacent dipoles are arranged antiparallel so that their unit cells and the material have zero macroscopic polarization in the absence of an external electric field. However, an externally applied electric field of sufficient magnitude can induce a phase transition to a ferroelectric (FE) phase with a polar space group and ordered parallel dipole moments to build a non-zero macroscopic polarization [1–6]. If this transition is reversible, the material switches back to the AFE phase when the electric field is reduced below the critical electric field. The reversibility of the electric field-induced phase transition realizes the double hysteresis loop, which is a fingerprint and characteristic of AFEs. The negative electrocaloric effect [7–9], an increase of the dielectric permittivity with an increasing electric field [10–13], high strain response [14], high energy storage density [15], and negative capacitance [16] are functional properties that are closely related to the peculiar polar order of the AFE ground state and the presence of the electric field-induced phase transition. Hence, the applicability of AFEs ranges from pulse-power capacitors [17], DC-link capacitors for power electronics [18], electromechanical actuators [19], capacitor memory cells [20,21], voltage signal amplifiers to solid-state coolants [9], and more. Despite their versatile applicability, AFEs are still under-researched compared to their FE counterpart. In particular, the relations between the AFE polar ground state, field-induced phase transition, and functional properties are not fully explored and understood. Moreover, emerging new applications, such as environmentally friendly solid-state cooling or neuromorphic computing, require a clear picture of the underlying physical mechanisms for designing materials with improved performances.

To enhance the functional properties in classical FEs, different approaches, such as chemical modification [22], preparation of solid solutions with the morphotropic phase boundary [23,24], preparation of composites [25], application of external and internal mechanical stress [26], and the concept of criticality [27,28], were developed and investigated. Chemical modification of canonical AFEs: $PbZrO_3$ [29], $AgNbO_3$ [30], and $NaNbO_3$ [31] is the most common approach to investigate the formation and stabilization of the AFE structure and its properties. It is well known that the temperature and nature of the inter-ferroelectric, ferroelectric-to-paraelectric [32], and relaxor-to-ferroelectric phase transitions change with the external electric field [27]. Under the electric field, the first-order phase transition can be changed to the second-order, and the critical electric field and the temperature of the crossover between the first- and second-order phase transitions define the critical point. Furthermore, if the second-order transition point is a singular point that terminates the line of the first-order phase transitions, the point is called the critical end point above which a supercritical behavior is observed [27]. In a supercritical regime, the dielectric susceptibility and the heat capacity become non-critical and smeared out due to the energetic equivalence between the phases. At the critical end point, the dielectric susceptibility and the heat capacity diverge, leading to an anomalous enhancement of functional properties such as the piezoelectric and electrocaloric responses, as well as the energy storage density [28,33]. Since the AFE–FE phase transition is induced at a sufficiently high electric field, it is anticipated that the electric field can modify the AFE–FE phase transition and consequently change the functional properties of the AFE.

To demonstrate the above hypothesis, we investigated the FE–AFE and AFE–PE phase transitions in antiferroelectric ceramics utilizing dielectric spectroscopy. The analysis was exemplarily conducted on the $(Pb,Nb)(Zr,Sn,Ti)O_3$ system, which represents one of the most widely studied antiferroelectrics with high-energy storage properties. The temperature-dependent dielectric permittivity was measured under various electric fields and the detected dielectric anomalies were used to construct an electric field–temperature ($E-T$) phase diagram. The divergent behavior of the dielectric permittivity was analyzed to identify the position of the critical point. The dielectric and polarization responses as a function of the electric field were measured to calculate the dielectric tunability and energy storage density.

II. EXPERIMENTAL SECTION

The AFE ceramics with chemical formula $Pb_{0.99}Nb_{0.02}[(Zr_{0.57}Sn_{0.43})_{0.92}Ti_{0.08}]_{0.98}0_3$ (abbreviated as PNZST) was prepared by the mixed-oxide route, as described elsewhere [34]. The ceramic sample was ground to a thickness of 230 μm and covered with sputtered gold electrodes with a diameter of 1.5 mm on the sample's planar surfaces. Two thin copper wires were attached with a silver paste to provide electrical contacts. The dielectric permittivity was obtained during heating with a rate of 1 K min^{-1}, using a precision LCR meter (Keysight Agilent E4980A, Keysight Technologies, USA). The dielectric permittivity under the DC bias field was measured using a standard external electrical circuit with two capacitors. The capacitors serve as blocking capacitors to prevent damage to the impedance analyzer by the high DC voltage and current. In order to avoid any possible history-dependent effects, the sample was heated to 430 K for 15 min and then cooled under an external bias electric field to 240 K, i.e., field-cooled–field-heated protocol was used. The temperature-dependent polarization measurements under various external bias electric fields were performed with an electrometer (Keithley 6517B, Keithley Instruments USA), using the same protocol as for the dielectric measurement, except that the heating rate was 2 K min^{-1}.

In addition to temperature-dependent measurements, the dielectric permittivity and polarization were measured as a function of the electric field at various fixed temperatures. The sample was heated up to 430 K and then cooled and stabilized at the measurement temperature within ±2 mK to avoid any possible history-dependent effects of previous measurements. During dielectric permittivity and polarization measurements, the electric field was linearly cycled with a frequency of 1 mHz between ±35 and ±40 kV cm^{-1}, respectively. The dielectric permittivity was measured with a 1 V AC signal at a frequency of 1 kHz.

The third harmonic of the dielectric response was measured at zero electric field with a 20 V AC signal during a heating run with a rate of 1 K min^{-1}, using a dynamic signal analyzer (HP35665A, Keysight Technologies, USA). The ε_3' denotes the real part of the third harmonic of the dielectric permittivity.

III. RESULTS AND DISCUSSION

The investigated composition of PNZST ceramics possesses a rhombohedral ferroelectric phase at low temperatures, which transforms upon increasing the temperature into a tetragonal AFE phase at ≈304 K, a paraelectric (PE) multicell cubic phase at ≈411 K, and a single-cell cubic phase at ≈453 K [14,35]. The temperature evolution of the phases and their transition temperatures are very sensitive to thermal and electrical treatment history. Figure 1(a) shows the temperature evolution of the dielectric permittivity between 240 and 430 K under selected external electric fields (all dielectric permittivity measurements are shown in Fig. S1(a) in the Supplemental Material [36]). FE–AFE and AFE–PE phase transition temperatures were determined from the first and the second peak of the imaginary component of the complex dielectric permittivity, respectively (see Fig. S1(b) in the Supplemental Material [36]). The sequence of phase transitions and their temperatures at zero electric field, $\mathrm{FE} \xrightarrow{297\,K} \mathrm{AFE} \xrightarrow{408\,K} \mathrm{PE}$, are in good agreement with the literature [14,37]. By applying an external electric field, the FE–AFE and AFE–PE transition temperatures are shifted. The FE–AFE transition temperature increases, while the AFE–PE transition temperature decreases with an increasing electric field. The transition temperatures of the FE–AFE and AFE–PE transitions shift to 369.7 and 395.9 K at an electric field of 21 kV cm^{-1}, respectively. By further increasing the electric field, the transition anomalies finally merge at 25 kV cm^{-1}.

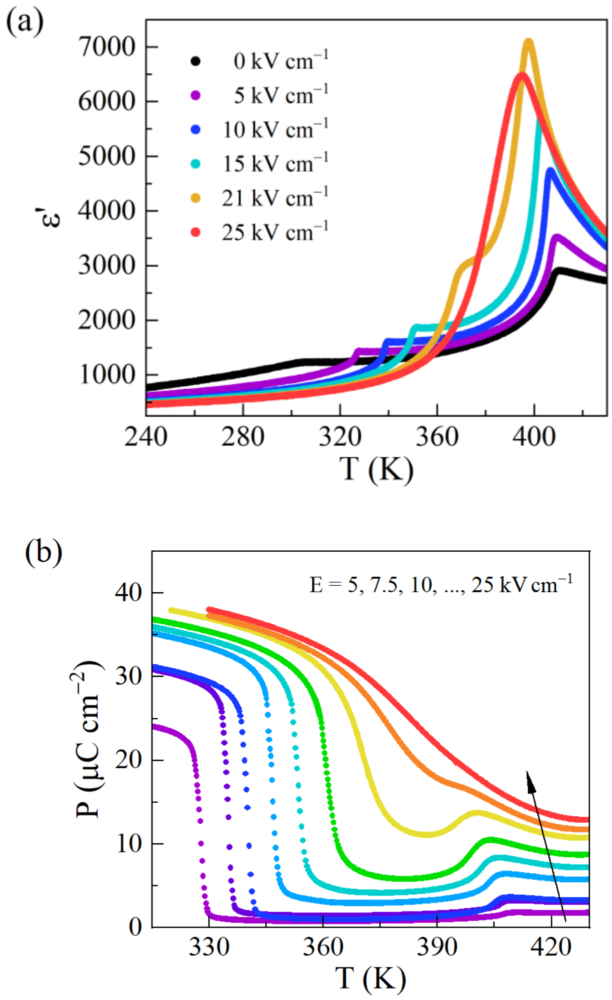

FIG. 1. (a) Real part of dielectric permittivity as function of temperature measured at 1 kHz and various electric fields. Only dielectric response for representative electric fields is shown. (b) Temperature evolution of macroscopic polarization measured at electric fields from 5 to 25 kV cm^{-1} in steps of 2.5 kV cm^{-1}. Arrow shows direction of increased electric field.

The FE–AFE and AFE–PE transition temperatures obtained from dielectric measurements coincide well with the sharp drop of polarization at lower temperatures and the anomaly at higher temperatures depicted in Fig. 1(b). The sharp drop of macroscopic polarization at the FE–AFE transition corroborates the first-order nature of the transition as demonstrated in Ref. [37]. The applied electric field not only shifts the transition temperatures but also changes the evolution of polarization. The FE–AFE transition is sharp and discontinuous at low electric fields, whereas it becomes continuous at 22.5 kV cm^{-1} and smeared and suppressed above 22.5

kV cm^{-1}, suggesting a supercritical behavior and the existence of a critical end point. The non-zero macroscopic polarization in the AFE phase indicates that the FE–AFE transition is not fully reversible, and the remains of the FE phase persist under the electric field, or a so-called ferrielectric state is formed [37–40]. In this state, the antiparallel sublattice polarizations do not cancel each other out due to the favorable orientation of the polarization in the direction of the applied electric field.

Upon approaching the AFE–PE transition temperature, the polarization exhibits an anomaly that shifts toward lower temperatures with an increasing electric field. The anomaly observed at the AFE-PE phase transition temperature could be a consequence of the conductivity effect. Typically, at the phase transition the resistance of the ferroelectric material drops, which manifests itself in the increase of the dielectric loss. While the anomaly can be attributed to the AFE–PE transition, its behavior does not reveal any indication about the nature of the AFE–PE phase transition. Therefore, we measured the third harmonic component of the dielectric permittivity. It has been predicted by the thermodynamic theory and demonstrated experimentally that the third harmonic changes its sign at the Curie temperature for the second-order phase transition, whereas for the first-order transition, the sign remains positive [41]. The sign of the measured third harmonic of PNZST ceramics (see Fig. S2 in the Supplemental Material [36]) does not change at the AFE–PE transition temperature; hence, the transition is of the first order. Therefore, the phase transition can change to the secondorder under an externally applied electric field.

The divergent nature of the dielectric permittivity was analyzed to determine the electric field and the temperature of the critical end points that terminate the lines of the first-order FE–AFE and AFE–PE phase transitions. To identify the divergent nature of the dielectric permittivity at the FE–AFE phase transition, the background of the dielectric response was fitted to the universal scaling ansatz [42]

$$\varepsilon' = C\tau^{-\gamma}(1 + a_{\varepsilon}\tau^{\Delta}) + D. \tag{1}$$

Here, C is the Curie constant, $\tau = \frac{(T - T_C)}{T_C}$ is the reduced temperature, γ is the universal scaling exponent, a_{ε} is the system-independent amplitude, Δ is an additional universal exponent, and D is the background dielectric permittivity. The background of the dielectric response fitted to the universal scaling ansatz for $E = 10$ kV cm^{-1} is presented in Fig. 2(a).

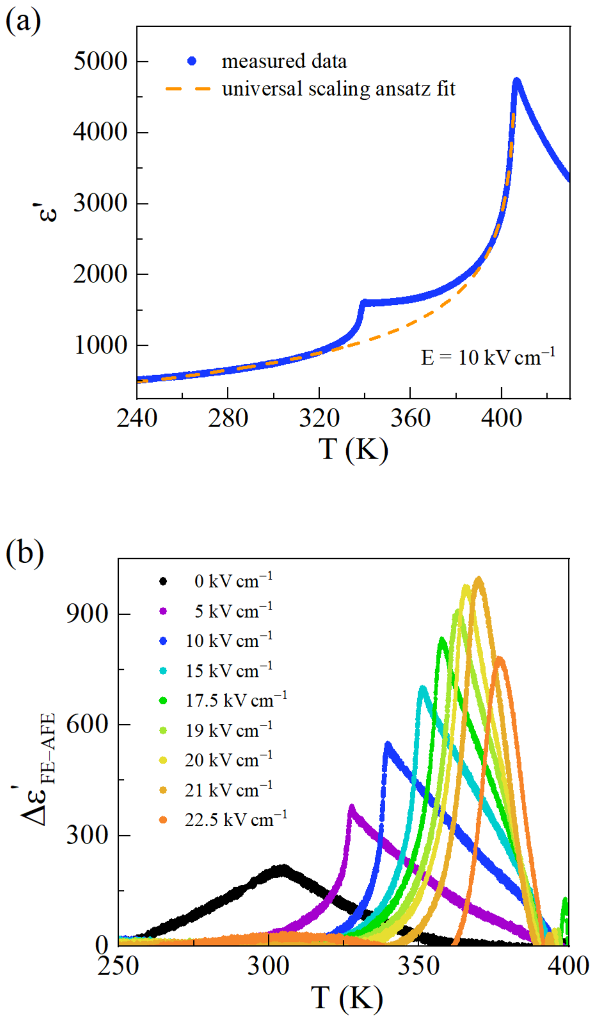

FIG. 2. (a) Ddielectric response measured at 10 kV cm^{-1}. Dashed line represents fit to universal scaling ansatz. (b) Dielectric anomaly of dielectric permittivity around FE–AFE phase transition, after fitted background was subtracted from measured data. Maximum dielectric response of FE–AFE phase transition is determined at 21 kV cm^{-1} and 369.7 K.

The fitted background response was subtracted from the measured dielectric response to determine the electric field at which the dielectric permittivity at the FE–AFE transition exhibits the maximum value. Figure 2(b) shows the subtracted dielectric response around the FE–AFE phase transition. The dielectric response at the FE–AFE transition increases under higher electric fields and exhibits the maximum value at 21 kV cm^{-1}. Further increasing the electric field leads to a suppressed and smeared dielectric response at the FE–AFE phase transition. Similarly to the FE–AFE transition, the AFE–PE phase transition also exhibits an enhanced dielectric response at 21 kV cm^{-1} and a smeared and suppressed dielectric response at higher electric fields [see Fig. 1(a)].

The analyzed dielectric response at FE–AFE and AFE–PE phase transitions demonstrates a typical behavior anticipated for a critical end point and a supercritical regime. It can be concluded that the lines of the first-order FE–AFE and AFE–PE phase transitions terminate in two critical end points located at E_{CP}^{FE-AFE} = 21 kV cm^{-1}, T_{CP}^{FE-AFE} = 369.7 K and E_{CP}^{AFE-PE} = 21 kV cm^{-1}, T_{CP}^{AFE-PE} = 395.9 K, respectively. The temperature stability of FE, AFE, and PE phases under various electric fields are represented in an electric field–temperature ($E-T$) phase diagram depicted in Fig. 3, with locations of both critical end points denoted by stars. Above the electric field of the critical end points, both transitions exhibit supercritical behavior. The FE–AFE phase transition merges with the AFE–PE phase transition at an electric field of 25 kV cm^{-1} and a temperature of 387.8 K.

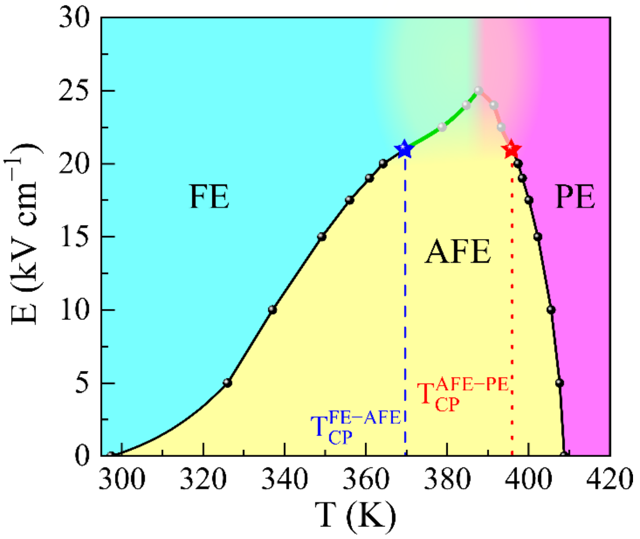

FIG. 3. Eelectric field–temperature phase diagram of antiferroelectric PNZST ceramics. Solid lines represent first-order FE–AFE and AFE–PE transition lines, which are terminated by critical end points marked with stars. Above critical end points, both transitions exhibit supercritical behavior. FE–AFE and AFE–PE phase transitions merge at 25 kV cm^{-1} and 387.8 K.

In contrast to classical ferroelectrics, the dielectric permittivity in AFEs increases with an increasing electric field. This peculiar behavior of the dielectric permittivity under the applied electric field is of high interest for developing capacitors for high-power electronics. Figures 4(a), 4(b), and 4(c) depict one of the main characteristics of these devices, namely the dielectric response as a function of the electric field around 343, 373, and 395 K, respectively. The selected temperatures represent the dielectric hysteresis response with the first-order AFE–FE phase transition, in the vicinity of the FE–AFE critical end point, and in the vicinity of the AFE–PE critical end point, respectively. The evolution of the dielectric permittivity as a function of the electric field at ≈343 K [see Fig. 4(a)] exhibits a sluggish increase with an increasing electric field, which becomes steeper upon approaching the first-order AFE–FE phase transition. After the FE phase is induced, a sharp decrease in the dielectric permittivity is observed, which is attributed to the poled FE state. In the vicinity of the FE–AFE critical end point temperature, the increase of the dielectric permittivity at low electric fields becomes faster and its enhancement at the field-induced AFE–FE phase transition temperature is larger [see Fig. 4(b)]. Moreover, in the vicinity of the AFE–PE critical end point temperature, the increase of the dielectric permittivity becomes even faster and exhibits the largest enhancement [see Fig. 4(c)].

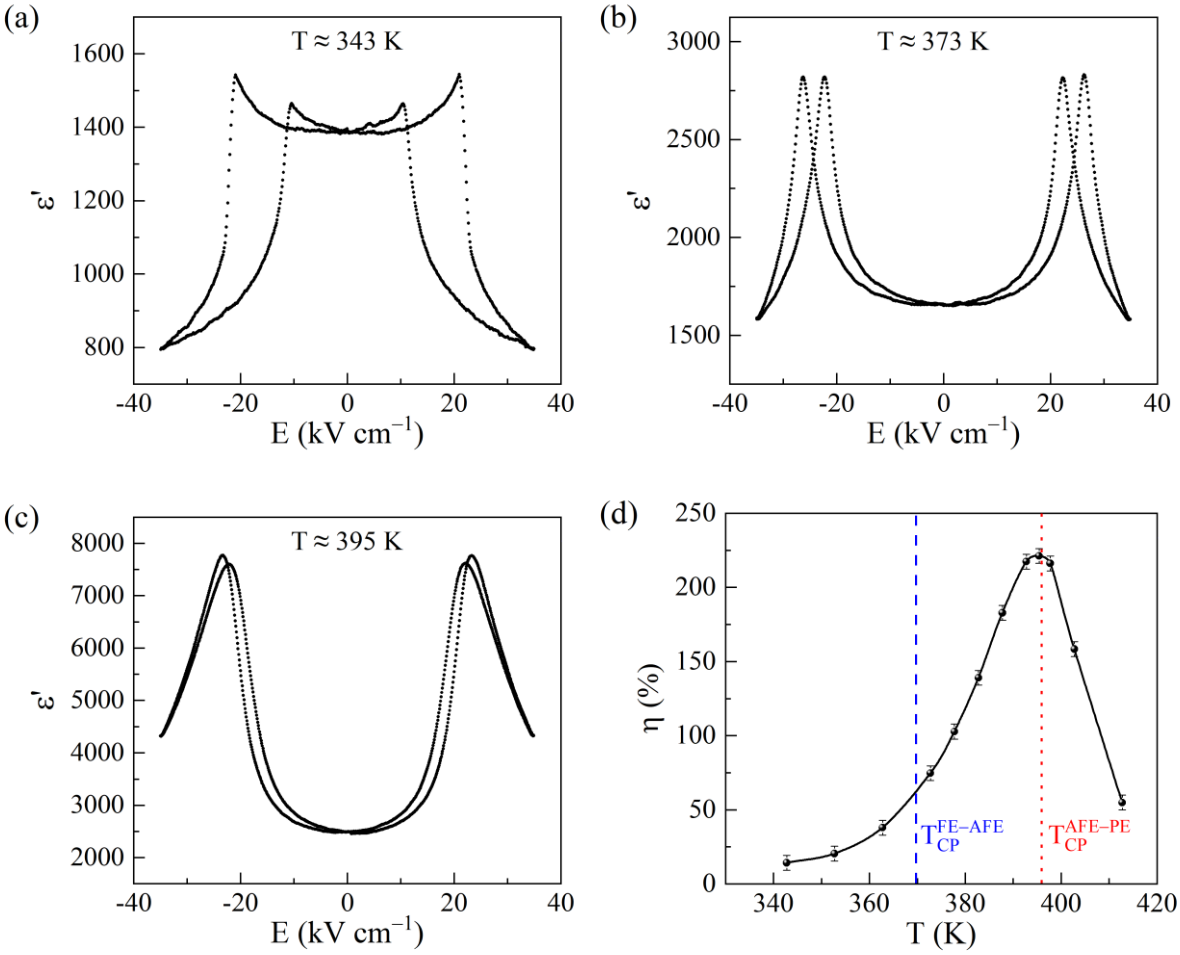

FIG. 4. (a), (b), and (c) Evolution of dielectric permittivity as a function of electric field during second measurement loop in PNZST at representative temperatures involving first-order AFE–FE phase transition, FE–AFE critical end point, and AFE–PE critical end point, respectively. (d) Tunability of dielectric response as function of temperature. Dashed and dotted lines represent temperatures of FE–AFE and AFE–PE critical end points, respectively.

To understand the role of both critical end points on the dielectric enhancement with an applied electric field, the dielectric tunability was calculated at various temperatures. The dielectric tunability, η, is defined as

$$\eta = \frac{\varepsilon'_{E_{AFE-FE}} - \varepsilon'_{E=0}}{\varepsilon'_{E=0}} \times 100\%, \qquad (2)$$

where $\varepsilon'_{E_{AFE-FE}}$ is the dielectric permittivity at the electric field of the AFE–FE phase transition and $\varepsilon'_{E=0}$ is the dielectric permittivity at zero electric field. Note that the numerator of Eq. (2) differs from the conventional equation for tunability used in dielectrics; here, the $\varepsilon'_{E_{AFE-FE}}$ and $\varepsilon'_{E=0}$ are switched, which satisfies the condition that the dielectric permittivity increases with the electric field and gives positive value for the tunability. The data for the calculations were extracted from the second measurement loop. The temperature-dependent tunability of the dielectric permittivity is depicted in Fig. 4(d). In the temperature range of the first-order AFE–FE phase transition, i.e., between 340 and 370 K, the dielectric tunability is between 15 and 60%. However, a strong enhancement of the tunability for a factor larger than 2 (221%), is obtained at ≈395 K. Such an enhancement of the dielectric permittivity by far exceeds the tunability values (88%) reported for ferroelectric and relaxor systems [43]. The temperature of the maximum dielectric tunability lies in the proximity of the AFE–PE critical end point (395.9 K), which demonstrates that the AFE–PE critical end point plays a crucial role in the enhancement of the dielectric response under an applied electric field. We assume that the increased dielectric response at the temperatures of the critical end points is due to the flattening of the free energy potential, which allows easy polarization extension under small perturbation fields. Furthermore, since the critical end point terminates the line of the first-order phase transition above which the transition becomes supercritical, it is expected that the free energy surface also becomes spherically degenerate. Consequently, polarization can easily rotate between the degenerated phases, which is a well-known mechanism responsible for enhanced functional properties of ferroelectrics [44,45]. It should be stressed that the flattening of the free energy is also expected at the FE-AFE critical end point; however, the change in the polarization at the rotation between the FE and AFE phase is expected to be smaller in comparison to the polarization change between the AFE and PE phase.

We also investigated the energy storage density and its relation to both critical end points in the antiferroelectric PNZST ceramic. The recoverable energy storage density, W_{rec}, of a dielectric can be calculated by the equation [15]

$$W_{rec} = \int_{P_r}^{P_{max}} E dP, \tag{3}$$

where E is the applied electric field, P_{max} is the maximum polarization, and P_r is the remanent polarization. The energy storage density was determined by integrating the area between the upper branch of the polarization hysteresis loop and the polarization axis. Hence, the polarization hysteresis loops at different temperatures (see Fig. S3 in the Supplemental Material [36]) were measured to determine the W_{rec} at different temperatures.

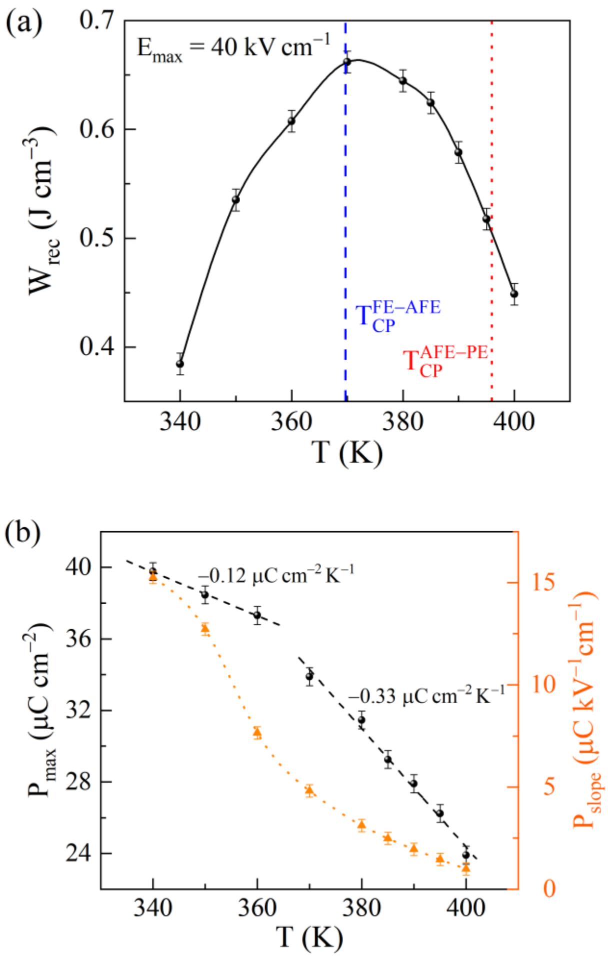

FIG. 5. (a) Temperature-dependent energy storage response of PNZST ceramics obtained at 40 kV cm^{-1}. Dashed and dotted lines represent temperatures of FE–AFE and AFE–PE critical end points, respectively. (b) Temperature evolution of the maximum polarization (full circles) and slope of polarization determined around AFE-FE phase transition (full triangles) of PNZST ceramics.

Figure 5(a) shows the temperature-dependent energy storage density of the antiferroelectric PNZST ceramics. The maximum energy storage response is observed at 370 K, which corresponds to the temperature of the FE–AFE critical end point. In contrast to the dielectric tunability, the FE–AFE critical end point plays a vital role in enhancing energy storage properties. To understand the enhancement of the recoverable energy density, the interplay between the maximum polarization, critical electric field, and the shape of the polarization hysteresis curve needs to be considered. Figure 5(b) depicts the temperature behavior of the maximum polarization and the slope of the polarization–electric field curve around the field-induced phase transition. Below the temperature of the FE–AFE critical end point, the maximum polarization exhibits a gradual decay with increasing temperature. A significant decrease of P_{max} at the FE-AFE critical end point and an increase of the decay rate above the FE–AFE critical end point is observed. Thus, according to Eq. (3), the energy storage should decrease with increasing temperature. However, with increasing temperature, the critical electric field for induction of the FE phase increases, which, in contrast to the decreasing polarization, contributes to the increase of the recoverable energy. Another critical parameter that influences the integrated area of recoverable energy density is the evolution curve of electric field-dependent polarization. The shape of the polarization evolution curve is determined by the slope of the polarization–electric field curve [see Fig. 5(b)]. The slope of the polarization curve at 340 K is steep, which indicates the first-order nature of the field-induced phase transition. With increasing temperature, the slope of the polarization curve decreases, which indicates the transition from the first to second-order phase transition. In addition, the decrease in the slope changes the shape of the polarization curve, which becomes more slanted above the FE-AFE critical end point. Hence, the enhancement of the recoverable energy density in the vicinity of the critical end point is a result of the interplay between the maximum polarization, critical electric field, and the shape of the polarization curve. In the vicinity of the FE-AFE critical end point, the polarization maximum reduces by ~15% compared to the polarization at 340 K, while the critical electric field increases by almost 53%. The slope of the polarization curve is reduced in the vicinity of the FE-AFE critical end point, but it does not result in a strong slanted polarization curve. The enhancement at the FE-AFE critical end point can be attributed to the relatively small reduction of the maximum polarization and a strong increase of the critical electric field. Furthermore, the decrease in the recoverable energy density above the FE-AFE critical end point is related to the stronger decrease in the maximum polarization, the slanted shape of the polarization curve, and a small change in the critical electric field.

IV. CONCLUSIONS

The ferroelectric-to-antiferroelectric and antiferroelectric-to-paraelectric phase transitions in PNZST ceramics were investigated using dielectric spectroscopy. It was demonstrated that the first-order transition lines of FE–AFE and AFE–PE phase transitions terminate in two separate critical end points. The locations of the FE–AFE and AFE–PE critical end points were determined to be at $E_{CP}^{FE-AFE} = 21$ kV cm^{-1}, $T_{CP}^{FE-AFE} = 369.7$ K and $E_{CP}^{AFE-PE} = 21$ kV cm^{-1}, $T_{CP}^{AFE-PE} = 395.9$ K, respectively. Above the critical end points, the dielectric response exhibits supercritical behavior, and at 25 kV cm^{-1} and 387.8 K, the transitions merge. Furthermore, the strong enhancement of the dielectric tunability was attributed to the proximity of the AFE–PE critical end point. It is suggested that the combination of flattening of the free energy potential at the critical end point and the degeneracy of FE, AFE, and PE phases are responsible for the enhanced dielectric response. On the other hand, the FE–AFE critical end point plays a crucial role in enhancing recoverable energy storage. The recoverable energy storage is defined by the relation between the maximum polarization and the electric field of the reversed ferroelectric-to-antiferroelectric phase transition; the optimal ratio between these two parameters is achieved at the FE–AFE critical end point, resulting in the best material performance. It has been demonstrated that the criticality, i.e., the presence of the critical end point, is an effective route to boost the functional properties of antiferroelectrics.

ACKNOWLEDGMENTS

VJ, VB, and NN would like to acknowledge funding of the Slovenian Research Agency under programs J2-4464 and P1-0125. LF and JK acknowledge the support of the Hessian State

Ministry for Higher Education, Research and the Arts under the LOEWE collaborative project FLAME (Fermi level engineering of antiferroelectric materials for energy storage and insulation systems).

[1] E. Sawaguchi, H. Maniwa, and S. Hoshino, *Antiferroelectric Structure of Lead Zirconate*, Phys. Rev. **83**, 1078 (1951).
[2] K. M. Rabe, *Antiferroelectricity in Oxides: A Reexamination*, in *Functional Metal Oxides: New Science and Novel Applications*, edited by S. B. Ogale, T. V. Venkatesan, and M. G. Blamire, First Edition (Wiley-VCH Verlag GmbH & Co. KGaA, Weinheim, Germany, 2013), pp. 221–244.
[3] C. Kittel, *Theory of Antiferroelectric Crystals*, Phys. Rev. **82**, 729 (1951).
[4] I. MacLaren, R. Villaurrutia, B. Schaffer, L. Houben, and A. Peláiz-Barranco, *Atomic-Scale Imaging and Quantification of Electrical Polarisation in Incommensurate Antiferroelectric Lanthanum-Doped Lead Zirconate Titanate*, Adv. Funct. Mater. **22**, 261 (2012).
[5] C. A. Randall, Z. Fan, I. Reaney, L.-Q. Chen, and S. Trolier-McKinstry, *Antiferroelectrics: History, Fundamentals, Crystal Chemistry, Crystal Structures, Size Effects, and Applications*, J. Am. Ceram. Soc. **104**, 3775 (2021).
[6] H. Liu, L. Fan, S. Sun, K. Lin, Y. Ren, X. Tan, X. Xing, and J. Chen, *Electric-Field-Induced Structure and Domain Texture Evolution in* $PbZrO_3$*-Based Antiferroelectric by in-Situ High-Energy Synchrotron X-Ray Diffraction*, Acta Mater. **184**, 41 (2020).
[7] P. D. Thacher, *Electrocaloric Effects in Some Ferroelectric and Antiferroelectric* $Pb(Zr, Ti)O_3$ *Compounds*, J. Appl. Phys. **39**, 1996 (1968).
[8] R. Pirc, B. Rožič, J. Koruza, G. Cordoyiannis, B. Malič, and Z. Kutnjak, *Anomalous Dielectric and Thermal Properties of Ba-Doped* $PbZrO_3$ *Ceramics*, J. Phys. Condens. Matter **27**, 455902 (2015).
[9] W. Geng, Y. Liu, X. Meng, L. Bellaiche, J. F. Scott, B. Dkhil, and A. Jiang, *Giant Negative Electrocaloric Effect in Antiferroelectric La-Doped* $Pb(ZrTi)O_3$ *Thin Films Near Room Temperature*, Adv. Mater. **27**, 3165 (2015).
[10] B. Jaffe, *Antiferroelectric Ceramics with Field-Enforced Transitions: A New Nonlinear Circuit Element*, Proc. IRE **49**, 1264 (1961).
[11] J. Wang, T. Yang, S. Chen, X. Yao, and A. Peláiz-Barranco, *DC Electric Field Dependence for the Dielectric Permittivity in Antiferroelectric and Ferroelectric States*, J. Alloys Compd. **587**, 827 (2014).
[12] Y. Feng, X. Wei, D. Wang, Z. Xu, and X. Yao, *Dielectric Behaviors of Antiferroelectric–Ferroelectric Transition under Electric Field*, Ceram. Int. **30**, 1389 (2004).
[13] L. Li, M. Spreitzer, D. Suvorov, and X. M. Chen, *Unique Dielectric Tunability of* $Pb_{0.99}[(Zr_{0.6}Sn_{0.4})_{0.94}Ti_{0.06}]_{0.98}Nb_{0.02}O_3$ *Antiferroelectric Ceramics*, J. Appl. Phys. **120**, 074109 (2016).
[14] X. Tan, C. Ma, J. Frederick, S. Beckman, and K. G. Webber, *The Antiferroelectric ↔ Ferroelectric Phase Transition in Lead-Containing and Lead-Free Perovskite Ceramics*, J. Am. Ceram. Soc. **94**, 4091 (2011).
[15] L. Zhao, Q. Liu, J. Gao, S. Zhang, and J.-F. Li, *Lead-Free Antiferroelectric Silver Niobate Tantalate with High Energy Storage Performance*, Adv. Mater. **29**, 1701824 (2017).

[16] M. Hoffmann, Z. Wang, N. Tasneem, A. Zubair, P. V. Ravindran, M. Tian, A. A. Gaskell, D. Triyoso, S. Consiglio, and K. Tapily et al., *Antiferroelectric Negative Capacitance from a Structural Phase Transition in Zirconia*, Nat. Commun. **13**, 1 (2022).

[17] J. P. Dougherty, *Cardiac Defibrillator with High Energy Storage Antiferroelectric Capacitor*, US5545184A (13 August 1996).

[18] K. Reichmann and T. Kainz, *Antiferroelectrics: Materials for New Ceramic Power Devices*, in *50th International Conference on Microelectronics, Materials and Devices* (2014).

[19] K. Uchino, *Antiferroelectric Shape Memory Ceramics*, Actuators **5**, 2 (2016).

[20] M. M. Vopson and X. Tan, *Four-State Anti-Ferroelectric Random Access Memory*, IEEE Electron Device Lett. **37**, 1551 (2016).

[21] D. H. Morris, U. E. Avci, and I. A. Young, *Anti-Ferroelectric Capacitor Memory Cell*, EP3576092B1 (23 December 2020).

[22] F. Li, M. J. Cabral, B. Xu, Z. Cheng, E. C. Dickey, J. M. LeBeau, J. Wang, J. Luo, S. Taylor, and W. Hackenberger et al., *Giant Piezoelectricity of Sm-Doped* $Pb(Mg_{1/3}Nb_{2/3})O_3$-$PbTiO_3$ *Single Crystals*, Science **364**, 264 (2019).

[23] B. Jaffe, R. S. Roth, and S. Marzullo, *Piezoelectric Properties of Lead Zirconate-Lead Titanate Solid-Solution Ceramics*, J. Appl. Phys. **25**, 809 (1954).

[24] M. Ahart, M. Somayazulu, R. E. Cohen, P. Ganesh, P. Dera, H. Mao, R. J. Hemley, Y. Ren, P. Liermann, and Z. Wu, *Origin of Morphotropic Phase Boundaries in Ferroelectrics*, Nature **451**, 7178 (2008).

[25] C. Zhao, S. Gao, T. Yang, M. Scherer, J. Schultheiß, D. Meier, X. Tan, H.-J. Kleebe, L.-Q. Chen, and J. Koruza et al., *Precipitation Hardening in Ferroelectric Ceramics*, Adv. Mater. **33**, 2102421 (2021).

[26] L. M. Riemer, K. V. Lalitha, X. Jiang, N. Liu, C. Dietz, R. W. Stark, P. B. Groszewicz, G. Buntkowsky, J. Chen, and S.-T. Zhang et al., *Stress-Induced Phase Transition in Lead-Free Relaxor Ferroelectric Composites*, Acta Mater. **136**, 271 (2017).

[27] Z. Kutnjak, J. Petzelt, and R. Blinc, *The Giant Electromechanical Response in Ferroelectric Relaxors as a Critical Phenomenon*, Nature **441**, 7096 (2006).

[28] F. Weyland, M. Acosta, J. Koruza, P. Breckner, J. Rödel, and N. Novak, *Criticality: Concept to Enhance the Piezoelectric and Electrocaloric Properties of Ferroelectrics*, Adv. Funct. Mater. **26**, 7326 (2016).

[29] D. Berlincourt, H. H. A. Krueger, and B. Jaffe, *Stability of Phases in Modified Lead Zirconate with Variation in Pressure, Electric Field, Temperature and Composition*, J. Phys. Chem. Solids **25**, 659 (1964).

[30] Z. Lu, W. Bao, G. Wang, S.-K. Sun, L. Li, J. Li, H. Yang, H. Ji, A. Feteira, and D. Li et al., *Mechanism of Enhanced Energy Storage Density in* $AgNbO_3$*-Based Lead-Free Antiferroelectrics*, Nano Energy **79**, 105423 (2021).

[31] M.-H. Zhang, H. Ding, S. Egert, C. Zhao, L. Villa, L. Fulanović, P. B. Groszewicz, g. Buntkowsky, H.-J. Kleebe, and K. Albe et al., *Tailoring High-Energy Storage* $NaNbO_3$*-Based Materials from Antiferroelectric to Relaxor States*, Nat. Commun. **14**, 1 (2023).

[32] N. Novak, R. Pirc, and Z. Kutnjak, *Impact of Critical Point on Piezoelectric and Electrocaloric Response in Barium Titanate*, Phys. Rev. B **87**, 104102 (2013).

[33] M. Porta, T. Lookman, and A. Saxena, *Effects of Criticality and Disorder on Piezoelectric Properties of Ferroelectrics*, J. Phys. Condens. Matter **22**, 345902 (2010).

[34] X. Tan, S. E. Young, Y. H. Seo, J. Y. Zhang, W. Hong, and K. G. Webber, *Transformation Toughening in an Antiferroelectric Ceramic*, Acta Mater. **62**, 114 (2014).

[35] H. Liu, Z. Zhou, Y. Qiu, B. Gao, S. Sun, K. Lin, L. Ding, Q. Li, Y. Cao, and Y. Ren et al., *An Intriguing Intermediate State as a Bridge between Antiferroelectric and Ferroelectric Perovskites*, Mater. Horiz. **7**, 1912 (2020).

[36] See Supplemental Material at [URL] for the temperature dependence of the linear and nonlinear dielectric response at all measured electric fields and the polarization hysteresis loops.

[37] N. Novak, F. Weyland, S. Patel, H. Guo, X. Tan, J. Rödel, and J. Koruza, *Interplay of Conventional with Inverse Electrocaloric Response in (Pb,Nb)(Zr,Sn,Ti)* O_3 *Antiferroelectric Materials*, Phys. Rev. B **97**, 094113 (2018).

[38] P. Tolédano and M. Guennou, *Theory of Antiferroelectric Phase Transitions*, Phys. Rev. B **94**, 014107 (2016).

[39] H. He and X. Tan, *Electric-Field-Induced Transformation of Incommensurate Modulations in Antiferroelectric* $Pb_{0.99}Nb_{0.02}[(Zr_{1-x}Sn_x)_{1-y}Ti_y]_{0.98}O_3$, Phys. Rev. B **72**, 024102 (2005).

[40] Z. Fu, X. Chen, Z. Li, T. Hu, L. Zhang, P. Lu, S. Zhang, G. Wang, X. Dong, and F. Xu, *Unveiling the Ferrielectric Nature of* $PbZrO_3$*-Based Antiferroelectric Materials*, Nat. Commun. **11**, 1 (2020).

[41] S. Miga and J. Dec, *Non-Linear Dielectric Response of Ferroelectric and Relaxor Materials*, Ferroelectrics **367**, 223 (2008).

[42] M. Seeger, S. N. Kaul, H. Kronmüller, and R. Reisser, *Asymptotic Critical Behavior of Ni*, Phys. Rev. B **51**, 12585 (1995).

[43] L. B. Kong, S. Li, T. S. Zhang, J. W. Zhai, F. Y. C. Boey, and J. Ma, *Electrically Tunable Dielectric Materials and Strategies to Improve Their Performances*, Prog. Mater. Sci. **55**, 840 (2010).

[44] H. Fu and R. E. Cohen, *Polarization Rotation Mechanism for Ultrahigh Electromechanical Response in Single-Crystal Piezoelectrics*, Nature **403**, 6767 (2000).

[45] A. A. Heitmann and G. A. Rossetti Jr., *Thermodynamics of Ferroelectric Solid Solutions with Morphotropic Phase Boundaries*, J. Am. Ceram. Soc. **97**, 1661 (2014).